Nanoscale

PAPER

View Article Online
View Journal

Published on 06 September 2019. Downloaded by Sungkyunkwan University on 9/30/2019 11:10:26 AM.

Check for updates

Cite this: DOI: 10.1039/c9nr04567h

Metallic contact induced van der Waals gap in a MoS_2 FET†

Changsik Kim,‡ Kwang Young Lee,‡ Inyong Moon, Sudarat Issarapanacheewin and Won Jong Yoo *

Received 29th May 2019,
Accepted 6th September 2019

DOI: 10.1039/c9nr04567h

rsc.li/nanoscale

Electrical metal contacts formed with 2D materials strongly affect device performance. Here, we used scanning transmission electron microscopy (STEM) and energy-dispersive spectroscopy (EDS) to characterize the interfacial structure formed and physical damage induced between MoS_2 and the most commonly used metals, Ti, Cr, Au, and Pd. We further correlated the electrical performance with physical defects observed at the 2D interfacial structure. The contact resistances were higher in the order of Ti, Au, Pd, and Cr contacts, but all 4-point probe mobilities measured with metals in contact with identical quadrilayer MoS_2 were ~65 cm^2 V^{-1} s^{-1}, confirming the reliability of the devices. According to the STEM and EDS analyses, the Ti contact gave rise to a van der Waals gap between the clean quadrilayer MoS_2 and the Ti contact. By contrast, Cr migrated into MoS_2 while Mo and S counter-migrated into the SiO_2 substrate. Au and Pd formed glassy layers that resulted in the migration of Mo and S into the Au and Pd electrodes. These interfacial structures between MoS_2 and contact metals strongly correlated with the electrical performance of 2D MoS_2 FETs, providing practical guidelines to form van der Waals contacts.

Introduction

Since its report in 2004, the two-dimensional (2D) material graphene has been studied because of its unique structure and properties.[1] Next-generation 2D materials, such as transition-metal dichalcogenides and black phosphorous, extend 2D applications substantially because of their tunable band gap.[2] With respect to future electronic applications, 2D materials have been demonstrated to function as channel materials in field-effect transistors (FETs), p–n junctions, inverters, memory devices, and microprocessors.[3–7] Among these 2D materials, molybdenum disulfide (MoS_2) is considered as one of the most promising materials because of its natural abundance, good chemical stability, and extendibility to wafer-scale synthesis,[8] in addition to its sizable band gap in the range 1.2–1.8 eV and an on/off current ratio as high as ~10^8.[9,10] Because of its 2D ultra-thinness and favorable properties, MoS_2 transistors exhibit excellent switching performance even with 1–4 nm channel lengths, without exhibiting a severe short-channel effect.[11]

In recent studies of 2D materials, electrical metal contacts have been found to present serious technical challenges. Mostly, researchers have deposited metals directly onto the top/surface of 2D materials to form metallic electrodes. From the early papers on graphene to recent reports of a "magic angle" graphene superlattice, such top metal contacts have been predominantly used.[1,12] However, the electrical contact between a metal and a 2D semiconductor interferes with researchers' ability to demonstrate the quantum mechanical performance unique to 2D devices, *e.g.*, quantum transport, superconductor, and valley transport devices.[13,14] In particular, the absence of surface dangling bonds at the 2D interfaces gives rise to a van der Waals tunnel barrier and weakens intralayer atomic bonding.[15,16] Surprisingly, semiconducting 2D materials cause high contact resistances, stubborn polarity, and an uncontrollable Schottky barrier height (SBH), which are related to strong Fermi-level pinning.[17,18] That is, if a van der Waals gap exists as a tunnel barrier at the interface, Fermi-level pinning is expected to be alleviated because of the reduced charge dipole between the metal and the semiconductor.[19,20] Apparently, the van der Waals gap, acting as a tunnel barrier, has not existed clearly at the interface between 2D materials and contacting metals. Atomic vacancies and defects can induce much stronger Fermi-level pinning than that theoretically expected.[17,21–24]

Several innovative approaches to achieving good metal contact have recently been proposed. A one-dimensional electrical contact gave rise to greatly improved electronic

SKKU Advanced Institute of Nano-Technology (SAINT), Sungkyunkwan University (SKKU), 2066, Seobu-ro, Jangan-gu, Suwon-si, Gyeonggi-do, 16419, Republic of Korea. E-mail: yoowj@skku.edu

†Electronic supplementary information (ESI) available. See DOI: 10.1039/c9nr04567h

‡These authors contributed equally to this work.

Published on 06 September 2019. Downloaded by Sungkyunkwan University on 9/30/2019 11:10:26 AM.

performance for graphene and Fermi level depinning enabling ambipolar performance for MoS_2.[25,26] Inserting hexagonal boron nitride (h-BN) or a polymeric dopant interlayer replacing a van der Waals gap can reduce the contact resistance and SBH between a metal and MoS_2.[27–30] Liu *et al.* reported that evaporated metals physically damage the MoS_2 surface, whereas a transferred metal that functions as a van der Waals contact on MoS_2 clearly contributes to Fermi-level de-pinning and to the formation of a van der Waals gap.[31] Wang *et al.* recently reported that gold-capped indium can also form a low-resistance van der Waals contact *via* direct metal deposition and post-annealing.[32]

In this work, we explored the interface formed between 2D materials and metals. Scanning transmission electron microscopy (STEM) and energy-dispersive spectroscopy (EDS) were used to investigate the atomic structure at the van der Waals interface, the physical damage that occurred during evaporation, and the existence of a van der Waals gap. Additionally, device properties of MoS_2 obtained from various metal contacts were examined *via* measurements of the electrical characteristics of MoS_2 FETs.

Results and discussion

Electrical characteristics of MoS_2 FETs

As metal electrodes, Ti, Cr, Au, and Pd were chosen to be tested and compared because these materials have been extensively used and studied.[13,16,17,31,33] Ti and Cr have relatively low metal work functions of approximately 4.5 eV and show good adhesion to SiO_2 substrates. In particular, Ti is known to react with MoS_2 and form an alloy at the interface.[34] However, Ti and Cr have lower conductivities than Au and Pd. Because Au and Pd have high metal work functions (>5 eV), they can be used in high-performance p-type transistors.[31,33] Unlike Ti, Au does not react with MoS_2.[13] To ensure good adhesion and conductivity, double-stack metals (Cr/Au, Ti/Au) are often used for forming contacts.[1,12,17] In terms of the metal work function and conductivity, we think that these metals can be very good candidates for investigating and comparing the electrical performance and physical interaction of metals with MoS_2, the detailed properties of the metals are summarized in Table S1.†

As shown in Fig. 1, we fabricated a MoS_2 transistor with various metals on an identical MoS_2 flake to ensure a fair comparison. We used TEM to observe the quadrilayer MoS_2 and characterize any physical damage that occurred during metal evaporation. The MoS_2 layers were exfoliated onto a 285 nm SiO_2 onto which a p++ Si substrate was used for global back gating. Plasma treatment was performed to etch the MoS_2 to obtain a device structure with the same length and width for each metal contact. Electrodes were patterned *via* electron-beam lithography using a poly(methyl methacrylate) (PMMA) mask. All four of the aforementioned metal electrodes with a 1 μm width had various channel lengths of 2, 4, and 8 μm for transfer line measurement (TLM), and these electrodes were also used for four-point probe (4pp) measurement for measuring the contact resistance (R_C) and the four-point probe mobility (μ_{4pp}) because the R_C is one of the most critical parameters for quantifying metal contact properties. All of the metal deposition processes were conducted at the same pressure and deposition rate because these parameters can affect the device performance.[35] The base pressure was 10^{-8} Torr, and the depo-

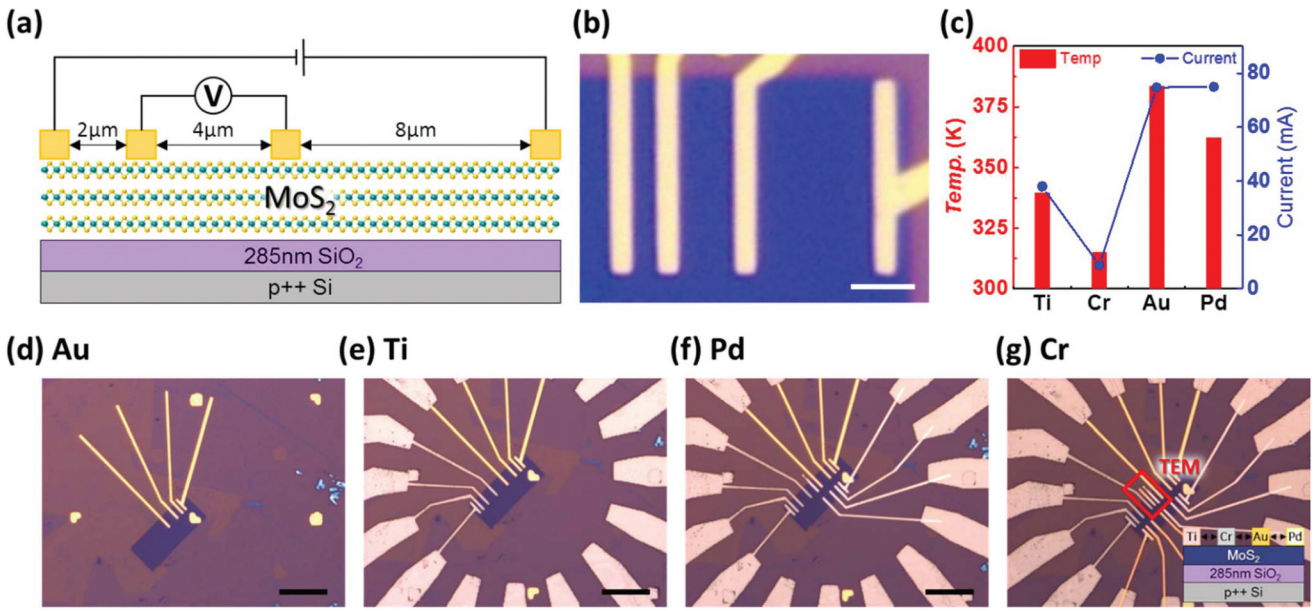

Fig. 1 Device structure and metal deposition process. (a) Schematic and (b) optical microscopy image of a MoS_2 transistor with TLM and 4pp configurations (scale bar is 5 μm). (c) Electron-beam current ($I_{E\text{-beam}}$) and temperature of each metal during evaporation. Optical microscopy images of a MoS_2 transistor after (d) Au, (e) Ti, (f) Pd, and (g) Cr deposition (scale bar is 20 μm). Inset: Ti, Cr, Au, and Pd metal on MoS_2 for TEM observation.

 This journal is © The Royal Society of Chemistry 2019

Published on 06 September 2019. Downloaded by Sungkyunkwan University on 9/30/2019 11:10:26 AM.

sition rate was varied in the range from 0.02 to 0.1 nm s^{-1}. We observed that the vacuum pressure during Au and Pd evaporation increased to 10^{-7} Torr while the deposition was carried out. We used only single-elemental metal layers instead of hybrid stacked metals (Ti/Au, Cr/Au) for the precise detection of the chemical composition by EDS. Fig. 1c shows the electron-beam current ($I_{\text{E-beam}}$) and temperature during evaporation. Au and Pd required electron beam currents and a temperature greater than those required by Cr and Ti. Note that when metals evaporate under vacuum, the vapor pressure and temperature of metal atoms are expressed by the Clausius–Clapeyron equation.[36] Based on the kinetic theory of ideal gases, we estimated the kinetic energy of each metal atom as shown in Fig. S1 and Table S2.† Fig. 1d–g show the metal deposition process in sequential order. The four different metals were deposited adjacently with a channel length of 1 μm for TEM observation, as shown in the inset of Fig. 1g. The details of all the fabrication processes are shown in Fig. S2.† Usually, devices were annealed to enhance the adhesion and also to remove residues after fabrication,[35] except the devices used for analyzing the pristine interface because post-annealing can change the interfacial atomic structure.[37]

After device fabrication, the electrical properties were measured under vacuum conditions. Fig. 2a–d show the measured drain current (I_D) *vs.* gate voltage (V_G) for the MoS_2 transistors with different channel lengths for each of the four metals. All of the obtained transfer curves show n-type behavior. Although all of the electrodes were formed on the identical MoS_2, the current levels of the Ti and Au contacts are much higher than those of the Cr and Pd contacts. The current level of the Cr contact is particularly low. The transfer curves in the logarithmic scale and the output curves are shown in Fig. S3.† In the output curves, only the Ti contact shows a linear slope, implying the formation of an ohmic contact; the Cr, Au, and Pd contacts exhibit Schottky contact behavior. The current levels of the Au and Ti contacts are similar, but their behaviors differ. On the basis of the transfer curves in Fig. 2, we calculated the two-terminal field-effect mobility using eqn (1). Note that two-terminal mobilities are dependent on the channel resistance and the contact resistance.

$$\mu = \frac{dI_D}{dV_G}\frac{L}{WV_DC_{OX}} \quad (1)$$

Here, L and W are the channel length and width, respectively, and C_{OX} is the capacitance of the dielectric oxide (1.15×10^{-8} F cm^{-2} for 285 nm SiO_2). All of the obtained mobilities and threshold voltages (V_{Th}) are shown in Fig. 3b. The threshold voltages were deduced from the linear fit of the transfer curves. A comparison of the two-terminal mobilities reveals that Ti exhibits the highest mobility, followed by Au, Pd, and Cr. A large variation in the mobility of Au is indicated by large error bars.

To extract the contact resistance, we used both measurements in the 4pp configuration and TLM. The contact resistance values (green squares) obtained from the 4pp configur-

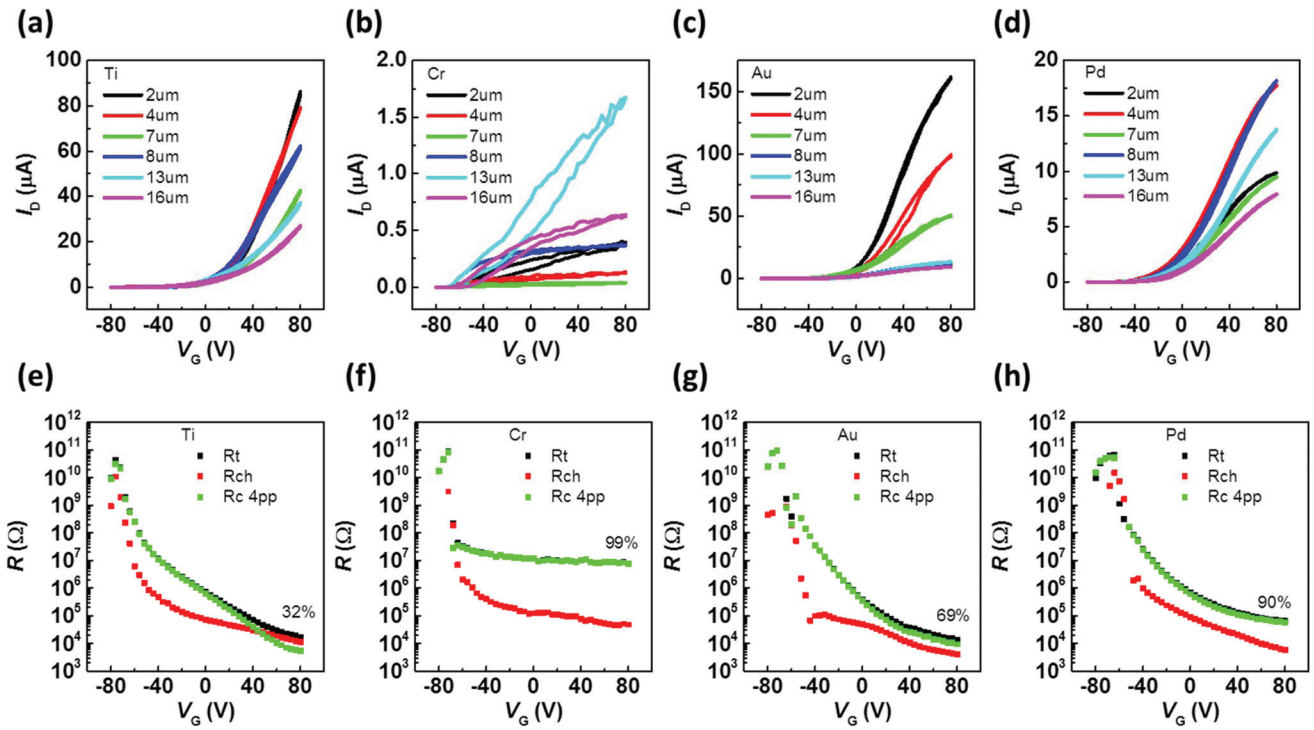

Fig. 2 Transfer and contact resistance characteristics of MoS_2 FET. (a)–(d) Transfer characteristics of the MoS_2 transistor with Ti, Cr, Au, and Pd metal contacts. All channels are 13 μm wide; the drain voltage (V_D) is 1 V. (e)–(h) The ratio between the contact resistance and the total resistance obtained from the 4pp configuration.

Published on 06 September 2019. Downloaded by Sungkyunkwan University on 9/30/2019 11:10:26 AM.

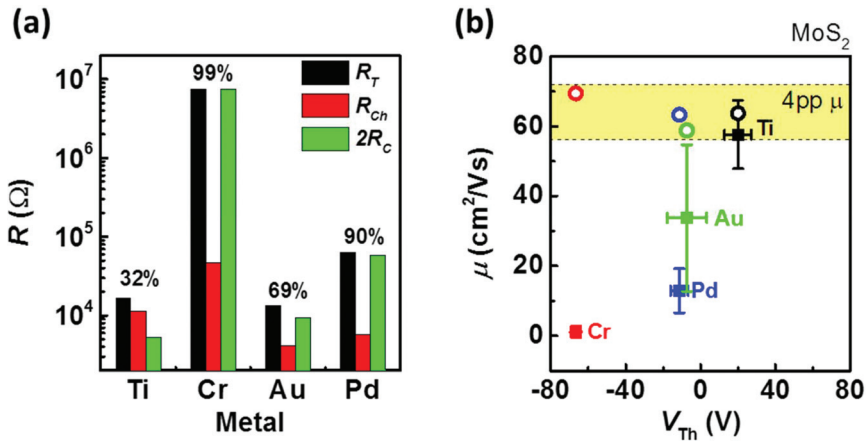

Fig. 3 Comparison of contact resistances and mobilities. (a) Percentages of contact resistance compared to the total resistance obtained when Ti, Cr, Au, and Pd contacts were used. (b) Mobilities and threshold voltages (V_{Th}) of MoS_2 transistors; hollow circles indicate the 4-point-probe mobilities in the yellow region.

ation are also plotted in Fig. 2e–h. For the 4pp measurements, the drain voltage was applied to the outer electrodes and the voltage drop between the inner electrodes was measured by comparing the applied voltage. On the basis of the measured voltage drop and current flow, we estimated both the channel resistance and the contact resistance. The contact resistance of Ti contacts measured *via* TLM was approximately 41 kΩ μm, with a small error bar and a value similar to the contact resistance obtained from 4pp measurements (32 kΩ μm). In the case of TLM, the linearly increasing trend with increasing channel length (L) was not clearly observed for metals other than Ti (Fig. S4†). This deviation from the linear behavior becomes more obvious for high contact resistances and introduces a larger measurement error. To indicate the deviation from linearity and the scattering of the TLM data, we show the error bars in the linear fitting used to obtain the contact resistances from TLM (red squares) in Fig. S4.† The contact resistances (black squares) obtained from measurements in the 4pp configuration are also plotted together. Other metal contacts show high contact resistances and large error bars compared with those of the Ti contact. The contact resistance of the Au contact from TLM even shows a negative value, implying that high contact resistances were extracted inaccurately by TLM. By contrast, when contact resistances were low, the TLM approach was found to be more accurate than the 4pp measurements because of the enhanced reliability in the linearity between the total resistance and the channel length.[35]

In Fig. 3a, the ratios of contact resistance from the Ti, Au, Pd, and Cr contacts with respect to the total resistance are 32%, 69%, 90%, and 99%, respectively. The high values of the ratio indicate that contact resistance dominates device performance, so it was difficult to obtain the linear dependence of the channel length on the current level: see Fig. 2. On the basis of these results, we calculated the 4pp mobilities by excluding the contact resistance and analyzed the electrical properties of the MoS_2 channel. Interestingly, the 4pp mobilities for all of the metals were similar at approximately 60–70 cm^2 $(V\ s)^{-1}$, as shown in Fig. 3b. This result indicates that, irrespective of the metals tested, the identical MoS_2 flake shows the same channel properties, confirming that our measurements are reliable.

TEM and EDS analyses

After performing electrical measurements, we deposited 30 nm-thick Pt onto all of the metal contacts and MoS_2 channels, followed by focused ion beam (FIB) milling for the cross-sectional characterization of the interface *via* TEM and EDS. Fig. 4 shows TEM pictures of the interfaces. Interestingly, the structures of MoS_2 under different metals differ substantially from each other even though an identical MoS_2 flake was used. The Ti contact shows a clear and uniform MoS_2 channel with a clear boundary (Fig. 4a), indicating that the structure of the MoS_2 layer was well preserved. However, in the case of the Cr contact, the MoS_2 layer was observed vaguely, likely because of the damage that occurred during the electron-beam evaporation of metal atoms. We took into consideration that the FIB milling can also damage 2D materials.[38] However, identical MoS_2 was used with various metal contacts; thus, the damage under the Cr contact was clearly not caused by the FIB milling. Unlike the other metal contacts, the Au and Pd contacts give rise to a glassy layer shown as a bump on the MoS_2 layer (Fig. 4c).[31] For the Au and Pd contacts, the MoS_2 layer maintained its layer structure; however, Au and Pd atoms apparently diffused into the layer, as reported by Liu *et al.*[31]

To analyze the chemical composition of the interface more clearly, we treated it with a high-energy electron beam shower, followed by STEM and EDS analyses. Fig. 5 shows the STEM images of the interface formed between each metal and MoS_2, along with the corresponding EDS results. The STEM images show clear quadrilayer MoS_2 under all of the metal contacts. Each EDS line profile was obtained along the vertical yellow lines in Fig. 5e–h. Notably, EDS recorded X-ray spectra gener-

 This journal is © The Royal Society of Chemistry 2019

Published on 06 September 2019. Downloaded by Sungkyunkwan University on 9/30/2019 11:10:26 AM.

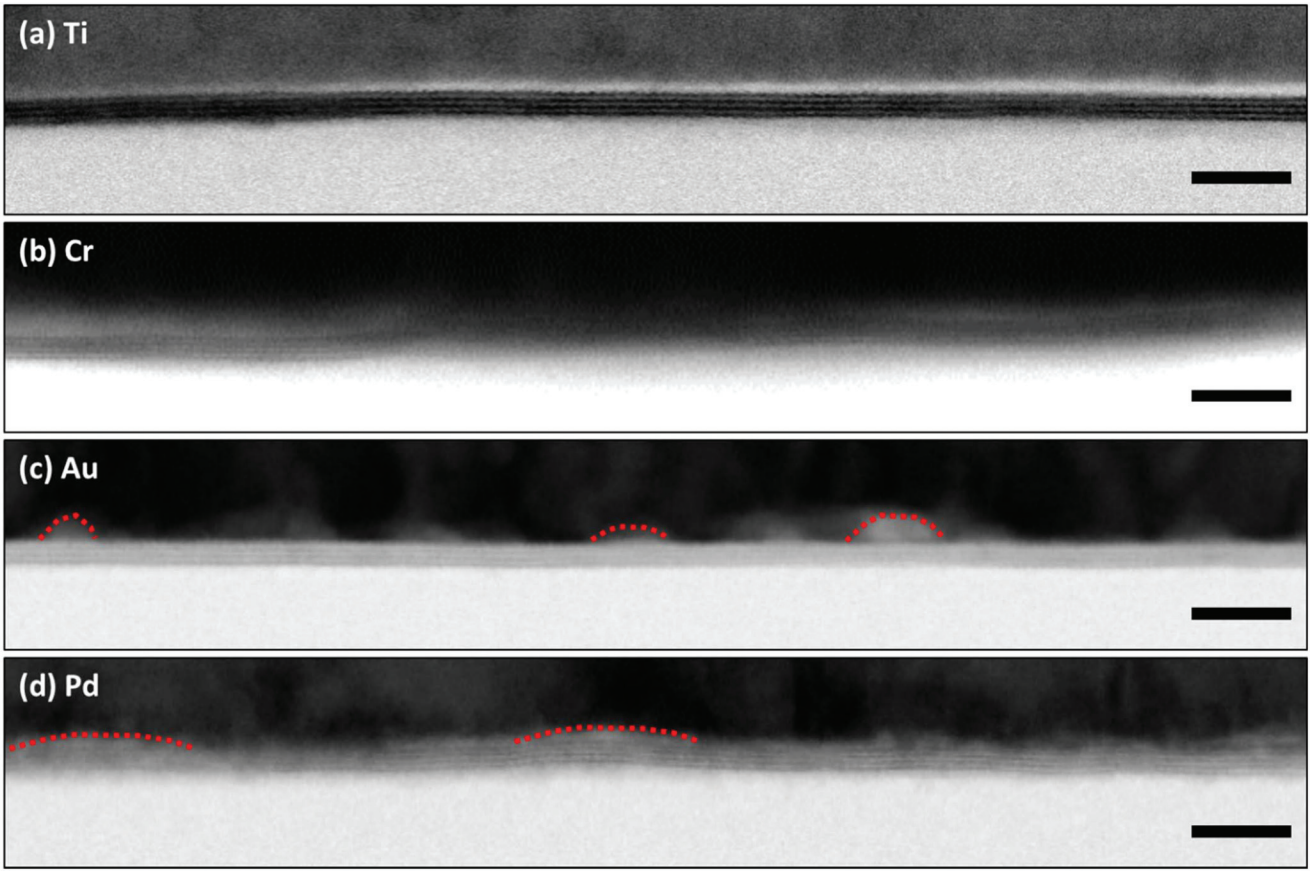

Fig. 4 Bright field TEM images of the interface formed between MoS_2 and contact metals. (a) Ti, (b) Cr, (c) Au, and (d) Pd. Scale bar is 10 nm. Red lines indicate the glassy layer between the MoS_2 layer and Au contact.

ated from the electron shell of an atom *via* a high-energy electron beam. In the case of the Mo, Pd, and Au atoms, the outer L electron shell was detected, whereas the inner K electron shell was detected for S, Ti, and Cr atoms.

Interestingly, the EDS results show different distributions of the various elements. In the case of the Ti contact, the boundary between the Ti metal and MoS_2 is clearly observed; however, the other metal atoms diffuse into the MoS_2 layer. These results are consistent with the previously discussed TEM results and electrical characteristics. In Fig. 5e, a clear boundary is observed between Ti and MoS_2 in the EDS and STEM images, indicating the presence of a van der Waals gap in the inset of Fig. 5a. According to the optimized geometry of the interface between a metal and 2D materials expected from density functional theory (DFT) calculations, the Au–MoS_2 contact gives rise to a van der Waals gap and the Ti–MoS_2 bond length is shorter than those between other metals and MoS_2, indicating that it is very likely that covalent bonding and ohmic contacts are formed.[13,15,24] However, the interfaces observed in this work are different from the ideal interface used for the DFT calculations. The formation of Ti_xS_y and TiO_2 from the reaction between MoS_2 and Ti was reported.[34] Fig. S5† shows detailed EDS and STEM. The overlap between the spectral peaks of Ti and S atoms was observed in a small part of the contact area. Detecting O atoms in TiO_2 was difficult because EDS can only detect atoms with high atomic numbers, and therefore electron loss energy spectroscopy (EELS) was adopted to detect oxygen, as shown in Fig. S6.† But the oxygen peak was hard to detect at the interface between Ti and MoS_2, unlike the clear oxygen peak from the SiO_2 substrate. McDonnell *et al.* reported that high vacuum ($\sim 10^{-6}$ mbar) conditions during Ti deposition prevented Ti atoms from reacting with MoS_2.[34] We expected this clean and clear interface between Ti and MoS_2 to result in high mobilities and a low contact resistance. As shown in Fig. 5f, the Cr atoms diffused into the MoS_2 layer and even further into the SiO_2 substrate; Mo and S atoms were also detected in the SiO_2 substrate. This result may indicate that Cr atoms "drag" Mo and S atoms into the SiO_2 substrate. Ti and Cr have similar properties, and both are well known to be effective adhesion layers; however, the TEM results and the electrical property measurements of FETs differ substantially between Ti and Cr. Au and Pd atoms are detected in the MoS_2 layer (Fig. 5g), but their concentration is lower than that of Cr atoms (Fig. 5f). Interestingly, Mo and S atoms are detected deep in the Au and Pd electrodes (Fig. 5g and h). During metal evaporation, the electron beam currents and temperature for Au and Pd are greater than those used for the other metals (Fig. 1c). We

Published on 06 September 2019. Downloaded by Sungkyunkwan University on 9/30/2019 11:10:26 AM.

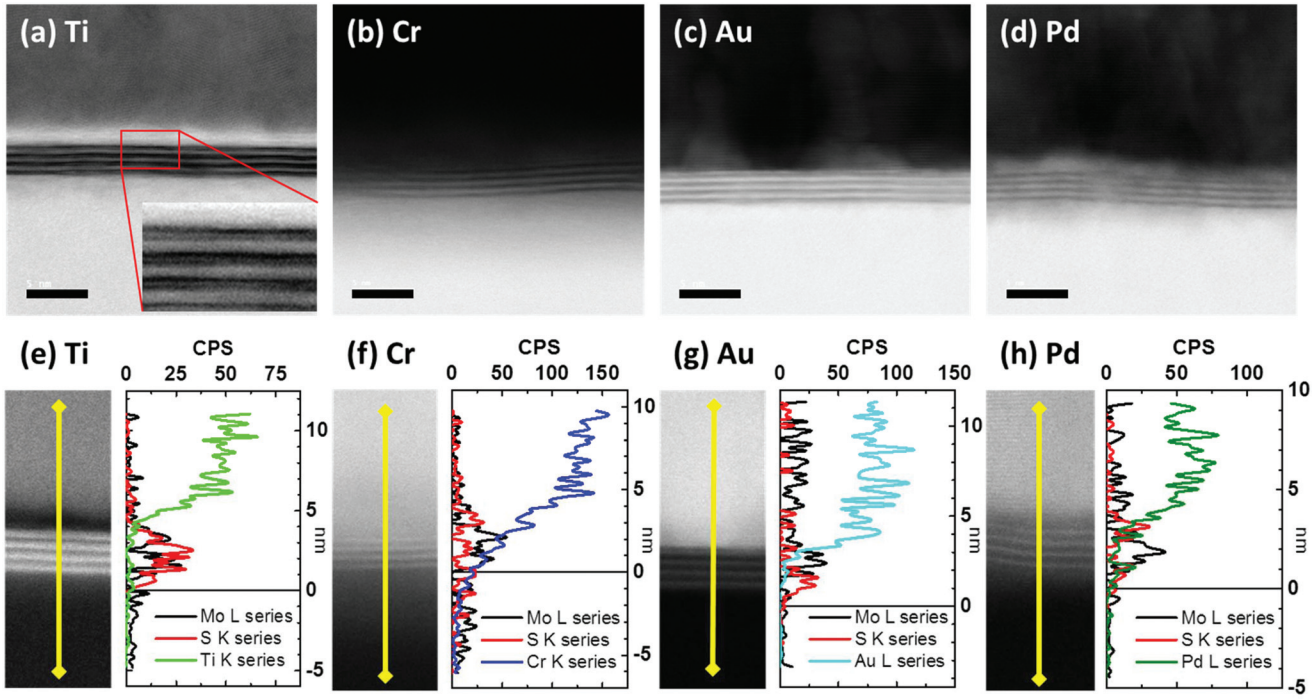

Fig. 5 STEM and EDS line profiles obtained from MoS_2 and contact metals. (a)–(d) Bright field STEM images of the interface between MoS_2 and Ti, Cr, Au, and Pd metal contacts. Scale bar is 5 nm. Inset: van der Waals gap exists between the MoS_2 layer and the Ti contact. (e)–(h) STEM images and EDS line profiles obtained from the interface between MoS_2 and various metals. The yellow lines in the STEM images indicate the EDS line profile. In the EDS graph, the origin is set to the interface between MoS_2 and the substrate.

speculate that the impinging Au and Pd atoms with high energy perturb the atomic structure of MoS_2, resulting in the relocation of Mo and S atoms and the formation of the glassy layer. As evidence, Cr atoms were also detected in the MoS_2 layer, whereas no Mo and S atoms were detected deep in the electrode. Because both Cr and Ti contacts were evaporated at a low electron-beam current, we propose that a high electron-beam current induces the relocation of MoS_2 deep into the electrode. More EDS results are shown in Fig. S5 to S9.† To compare the atomic distribution of Mo and S, we plotted all the EDS data for Mo and S atoms for each metal (Fig. S10†). The different distribution of Mo and S atoms under each metal is clearly observed. The Mo and S atoms penetrated the SiO_2 substrate along with Cr atoms during Cr deposition and appeared deep in the Au electrode during Au deposition, although S atoms were comparatively less abundant than Mo atoms.

Unlike the other metal contacts, the Au contact exhibits an unexpected glassy layer (Fig. 4c). Fig. S7† shows the STEM and EDS analyses on this layer. The atomic percentages in the glassy layer are shown in Table S3.† In the glassy layer, more Mo and S atoms are detected than Au atoms, meaning that Mo and S induced the formation of the glassy layer during Au deposition. Consequently, we speculated that the glassy layer induced the inhomogeneity of the Au contact. The atomic structures of metal compounds (Mo with Ti, Cr, Au, and Pd) can be analyzed *via* phase diagrams for binary mixtures (Fig. S11†), although the binary phase diagrams are based on 3D bulk crystal structures such as face-centered cubic, body-centered cubic, and hexagonal close-packed structures, whereas the crystal structure of 2H-MoS_2 is trigonal prismatic in a 2D plane. An alloy of Mo and Au is unlikely to form according to the EDS results. As reported in Table S3,† the atomic percentages of Mo, S, and Au in the middle of the Au electrode are 12%, 23%, and 64%, respectively. The ratio of S is higher than that of Mo. We speculate that gold sulfide (Au_xS_y) formed rather than the Mo–Au alloy. The metal oxide and sulfide compounds possibly formed through the reaction of MoS_2 with the metal electrodes are listed in Table S4.†

As shown in Fig. 3 and 5, the atomic structures under each metal contact are strongly correlated with the electrical performance when a metal serves as the electrode in a FET structure. In order to correlate electrical performance and interfacial structure, we drew band diagrams with or without van der Waals gap so as to enlighten carrier transport mechanisms more clearly, as shown in Fig. 6. The carrier transport at the interface between metal and semiconductor can be explained by thermionic emission and tunneling. See the ESI and Fig. S12† for more details. If a van der Waals gap exists at the interface, carrier transport is dominated by direct tunneling, rather than thermionic emission and Fowler–Nordheim (F–N) tunneling. Fig. 6c and f show an F–N plot to distinguish the carrier transport at the Ti and Pd contacts. In the case of the Ti contact, current shows little change for different temperatures, indicating that direct tunneling occurs dominantly across the van der Waals gap. However, in the case of the Pd contact, current shows strong temperature dependence with F–

 This journal is © The Royal Society of Chemistry 2019

Published on 06 September 2019. Downloaded by Sungkyunkwan University on 9/30/2019 11:10:26 AM.

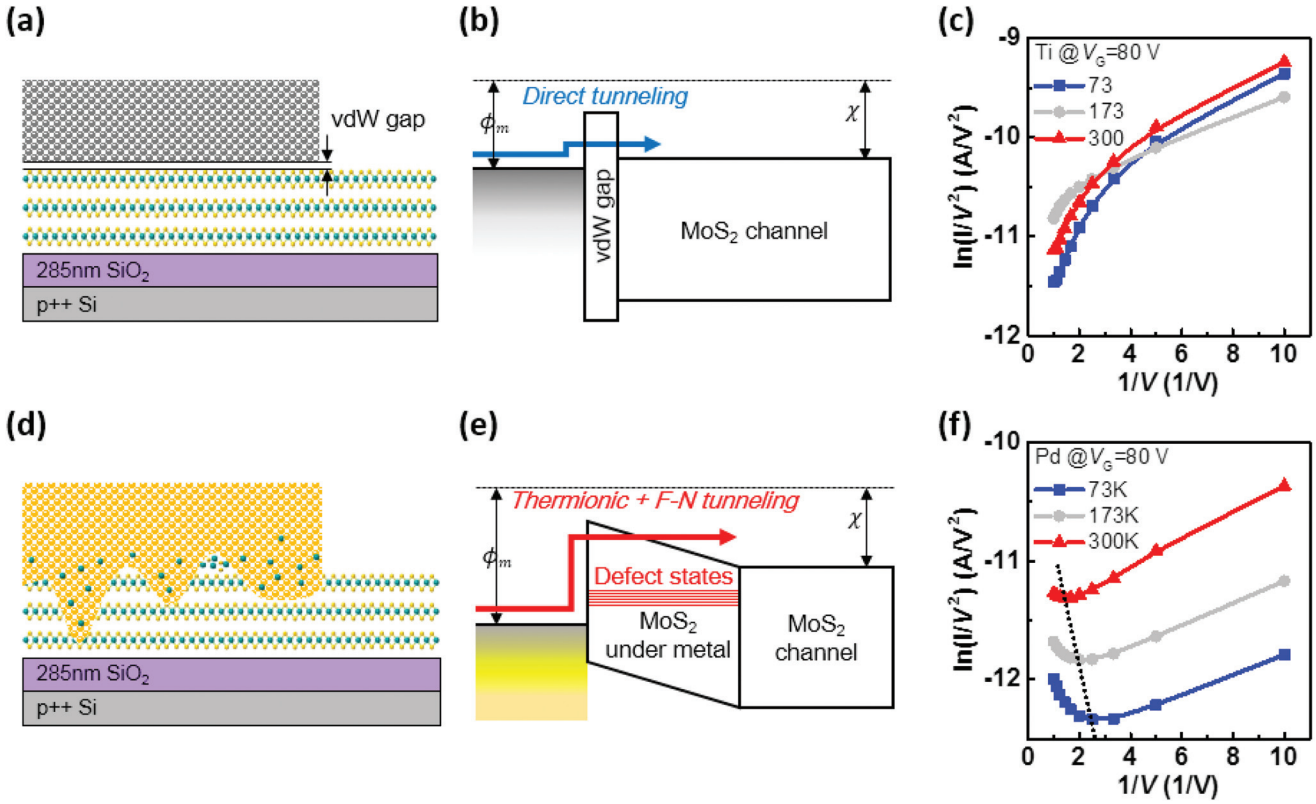

Fig. 6 Carrier transport mechanisms occurring at the metal and MoS_2 interface. (a), (d) Schematic diagrams of the interface with electrical metal contact. (b), (e) Band diagrams with and without the van der Waals gap. (c), (f) Fowler–Nordheim plots obtained from Ti and Pd contacts at the temperatures of 73, 173, and 300 K.

N tunneling behavior, indicating that thermionic emission and F–N tunneling occur dominantly without the van der Waals gap. That is, the Ti contact gives rise to the highest mobility with a clear interfacial van der Waals gap, whereas the other metal contacts give rise to damage of the MoS_2 layer, resulting in low electrical performance and a nonuniform interface.

From the perspective of Fermi level pinning, the effect of interfacial structures makes it difficult to predict the relationship between Schottky barrier height and metal work function. For the direct metal deposition on the surface of 2D materials, each metal formed a different interfacial structure which affects device performance more sensitively than its own work function and aggravates the Fermi level pinning of 2D materials.[17] However, when each metal has the same interfacial structure, *e.g.*, one dimensional edge contacts and transferred metal contacts, it is expected that its work function determines polarity and affects device performance, giving rise to a clear depinning effect.[26,31]

Conclusions

This study demonstrated the electrical properties of a MoS_2 transistor with Ti, Cr, Au, and Pd metal contacts, and their atomic structure at the interface was investigated by STEM and EDS from an identical MoS_2 flake. The mobility and contact resistance were obtained from transfer curves based on TLM and measurements in the 4pp configuration for each metal contact. The TEM and EDS analyses revealed four different types of interfacial atomic structures. The Ti contact gave rise to a clean and clear van der Waals gap between the metal and the MoS_2, whereas the other metal contacts diffused into the MoS_2 layer. In particular, the Cr contact penetrated and dragged Mo and S atoms into the SiO_2 substrate. The Au contact formed with a high electron-beam current formed a glassy layer and relocated Mo and S atoms deep into the electrode, giving rise to inhomogeneity in the mobilities of the device with an Au contact. These results imply that the interfacial structure formed during evaporation affects the electrical performance to a greater extent than the metal work function.

Experimental method

Exfoliation of the MoS_2 flake

MoS_2 was exfoliated by the mechanical exfoliation method. A 285 nm-thick SiO_2 layer on Si was used as a substrate; its dimensions were 1 cm × 1 cm. The SiO_2 was cleaned with acetone (C_3H_6O, 99.5%) and isopropanol (C_3H_8O, 99.5%) for 10 min under ultrasonic vibration. Afterwards, the SiO_2 surface was cleaned using O_2 plasma generated at 20 W for

Published on 06 September 2019. Downloaded by Sungkyunkwan University on 9/30/2019 11:10:26 AM.

1 min at 475 mTorr. Multilayer MoS_2 was exfoliated from bulk MoS_2 (HQ graphene) using sticky tape (3 M Scotch tape). The MoS_2 was baked at 100 °C for 10 min to obtain large-area flakes.[39]

Fabrication of MoS_2 FETs

To pattern electrodes and define the channel, PMMA (950 PMMA A6) was spin-coated onto MoS_2 (4000 rpm, 1 min) and annealed for 90 s at 453 K for hardening. Device structures were patterned *via* electron-beam lithography (JEOL JSM-7001F for SEM; Raith ELPHY Quantum for lithography). The MoS_2 channel was etched with SF_6/O_2 plasma (SF_6: 10 sccm, O_2: 30 sccm, 20 W, 60 s, 30 mTorr). Each metal electrode (Ti, Cr, Au, and Pd) had various channel lengths of 2, 4, and 8 μm, with a channel width of 12 μm and an electrode width of 1 μm for TLM and 4pp measurements. After patterning, the metal was deposited in an electron-beam evaporator (Korea Vacuum Tech, KVE-E2000). The electrical measurements were conducted using a semiconductor parameter analyzer (Agilent 4155C) in a vacuum chamber (MSTECH M6VC).

STEM and EDS analyses

The specimens were prepared in a FIB system (JEOL, JIB-4601F). Pt (30 nm) was deposited for passivation. All STEM and EDS analyses were performed using Cs-corrected high-resolution TEM (JEOL, JEM ARM 200F).

Conflicts of interest

There are no conflicts to declare.

Acknowledgements

This work was supported by the Global Research Laboratory (GRL) Program (2016K1A1A2912707) and Global Frontier R&D Program (2013M3A6B1078873), both funded by the Ministry of Science, ICT & Future Planning *via* the NRF.

Notes and references

1 K. S. Novoselov, *Science*, 2004, **306**, 666–669.
2 K. S. Novoselov, A. Mishchenko, A. Carvalho and A. H. Castro Neto, *Science*, 2016, **353**, aac9439.
3 L. Xie, M. Liao, S. Wang, H. Yu, L. Du, J. Tang, J. Zhao, J. Zhang, P. Chen, X. Lu, G. Wang, G. Xie, R. Yang, D. Shi and G. Zhang, *Adv. Mater.*, 2017, **1702522**, 1702522.
4 D. Li, M. Chen, Z. Sun, P. Yu, Z. Liu, P. M. Ajayan and Z. Zhang, *Nat. Nanotechnol.*, 2017, **12**, 901–906.
5 X. Liu, D. Qu, J. Ryu, F. Ahmed, Z. Yang, D. Lee and W. J. Yoo, *Adv. Mater.*, 2016, **28**, 2345–2351.
6 M. S. Choi, B. Cheong, C. H. Ra, S. Lee, J.-H. Bae, S. Lee, G.-D. Lee, C.-W. Yang, J. Hone and W. J. Yoo, *Adv. Mater.*, 2017, **29**, 1703568.
7 S. Wachter, D. K. Polyushkin, O. Bethge and T. Mueller, *Nat. Commun.*, 2017, **8**, 14948.
8 C. Ahn, J. Lee, H.-U. Kim, H. Bark, M. Jeon, G. H. Ryu, Z. Lee, G. Y. Yeom, K. Kim, J. Jung, Y. Kim, C. Lee and T. Kim, *Adv. Mater.*, 2015, **27**, 5223–5229.
9 B. Radisavljevic, A. Radenovic, J. Brivio, V. Giacometti and A. Kis, *Nat. Nanotechnol.*, 2011, **6**, 147–150.
10 G.-H. Lee, Y.-J. Yu, X. Cui, N. Petrone, C.-H. Lee, M. S. Choi, D.-Y. Lee, C. Lee, W. J. Yoo, K. Watanabe, T. Taniguchi, C. Nuckolls, P. Kim and J. Hone, *ACS Nano*, 2013, **7**, 7931–7936.
11 S. B. Desai, S. R. Madhvapathy, A. B. Sachid, J. P. Llinas, Q. Wang, G. H. Ahn, G. Pitner, M. J. Kim, J. Bokor, C. Hu, H.-S. P. Wong and A. Javey, *Science*, 2016, **354**, 99–102.
12 Y. Cao, V. Fatemi, S. Fang, K. Watanabe, T. Taniguchi, E. Kaxiras and P. Jarillo-Herrero, *Nature*, 2018, **556**, 43–50.
13 A. Allain, J. Kang, K. Banerjee and A. Kis, *Nat. Mater.*, 2015, **14**, 1195–1205.
14 D. Jena, K. Banerjee and G. H. Xing, *Nat. Mater.*, 2014, **13**, 1076–1078.
15 J. Kang, W. Liu, D. Sarkar, D. Jena and K. Banerjee, *Phys. Rev. X*, 2014, **4**, 031005.
16 C. Gong, L. Colombo, R. M. Wallace and K. Cho, *Nano Lett.*, 2014, **14**, 1714–1720.
17 C. Kim, I. Moon, D. Lee, M. S. Choi, F. Ahmed, S. Nam, Y. Cho, H.-J. J. Shin, S. Park and W. J. Yoo, *ACS Nano*, 2017, **11**, 1588–1596.
18 S. Das, H.-Y. Chen, A. V. Penumatcha and J. Appenzeller, *Nano Lett.*, 2013, **13**, 100–105.
19 D. Connelly, C. Faulkner, P. A. Clifton and D. E. Grupp, *Appl. Phys. Lett.*, 2006, **88**, 2002–2005.
20 R. T. Tung, *Appl. Phys. Rev.*, 2014, **1**, 011304.
21 Y. Guo, D. Liu and J. Robertson, *Appl. Phys. Lett.*, 2015, **106**, 173106.
22 S. McDonnell, R. Addou, C. Buie, R. M. Wallace and C. L. Hinkle, *ACS Nano*, 2014, **8**, 2880–2888.
23 P. Bampoulis, R. van Bremen, Q. Yao, B. Poelsema, H. J. W. Zandvliet and K. Sotthewes, *ACS Appl. Mater. Interfaces*, 2017, **9**, 19278–19286.
24 Y. Guo, D. Liu and J. Robertson, *ACS Appl. Mater. Interfaces*, 2015, **7**, 25709–25715.
25 L. Wang, I. Meric, P. Y. Huang, Q. Gao, Y. Gao, H. Tran, T. Taniguchi, K. Watanabe, L. M. Campos, D. A. Muller, J. Guo, P. Kim, J. Hone, K. L. Shepard and C. R. Dean, *Science*, 2013, **342**, 614–617.
26 Z. Yang, C. Kim, K. Y. Lee, M. Lee, S. Appalakondaiah, C. Ra, K. Watanabe, T. Taniguchi, K. Cho, E. Hwang, J. Hone and W. J. Yoo, *Adv. Mater.*, 2019, **1808231**, 1808231.
27 J. Wang, Q. Yao, C.-W. Huang, X. Zou, L. Liao, S. Chen, Z. Fan, K. Zhang, W. Wu, X. Xiao, C. Jiang and W.-W. Wu, *Adv. Mater.*, 2016, **28**, 8302–8308.
28 X. Cui, E.-M. Shih, L. A. Jauregui, S. H. Chae, Y. D. Kim, B. Li, D. Seo, K. Pistunova, J. Yin, J.-H. Park, H.-J. Choi, Y. H. Lee, K. Watanabe, T. Taniguchi, P. Kim, C. R. Dean and J. C. Hone, *Nano Lett.*, 2017, **17**, 4781–4786.

 This journal is © The Royal Society of Chemistry 2019

Published on 06 September 2019. Downloaded by Sungkyunkwan University on 9/30/2019 11:10:26 AM.

29 X.-X. Li, Z.-Q. Fan, P.-Z. Liu, M.-L. Chen, X. Liu, C.-K. Jia, D.-M. Sun, X.-W. Jiang, Z. Han, V. Bouchiat, J.-J. Guo, J.-H. Chen and Z.-D. Zhang, *Nat. Commun.*, 2017, **8**, 970.
30 D. Yue, C. Kim, K. Y. Lee and W. J. Yoo, *Adv. Funct. Mater.*, 2019, **29**, 1807338.
31 Y. Liu, J. Guo, E. Zhu, L. Liao, S. Lee, M. Ding, I. Shakir, V. Gambin, Y. Huang and X. Duan, *Nature*, 2018, **557**, 696–700.
32 Y. Wang, J. C. Kim, R. J. Wu, J. Martinez, X. Song, J. Yang, F. Zhao, A. Mkhoyan, H. Y. Jeong and M. Chhowalla, *Nature*, 2019, **568**, 70–74.
33 C. M. Smyth, L. A. Walsh, P. Bolshakov, M. Catalano, R. Addou, L. Wang, J. Kim, M. J. Kim, C. D. Young, C. L. Hinkle and R. M. Wallace, *ACS Appl. Nano Mater.*, 2019, **2**, 75–88.
34 S. McDonnell, C. Smyth, C. L. Hinkle and R. M. Wallace, *ACS Appl. Mater. Interfaces*, 2016, **8**, 8289–8294.
35 C. D. English, G. Shine, V. E. Dorgan, K. C. Saraswat and E. Pop, *Nano Lett.*, 2016, **16**, 3824–3830.
36 C. B. Alcock, V. P. Itkin and M. K. Horrigan, *Can. Metall. Q.*, 1984, **23**, 309–313.
37 J. Chen, Z. Feng, S. Fan, S. Shi, Y. Yue, W. Shen, Y. Xie, E. Wu, C. Sun, J. Liu, H. Zhang, W. Pang, D. Sun, W. Feng, Y. Feng, S. Wu and D. Zhang, *ACS Appl. Mater. Interfaces*, 2017, **9**, 30107–30114.
38 L. Yang, A. Charnas, G. Qiu, Y.-M. Lin, C.-C. Lu, W. Tsai, Q. Paduano, M. Snure and P. D. Ye, *ACS Omega*, 2017, **2**, 4173–4179.
39 Y. Huang, E. Sutter, N. N. Shi, J. Zheng, T. Yang, D. Englund, H.-J. Gao and P. Sutter, *ACS Nano*, 2015, **9**, 10612–10620.